

Communication

Improving Interfacial Charge-Transfer Transitions in Nb-Doped TiO₂ Electrodes with 7,7,8,8-Tetracyanoquinodimethane

Reo Eguchi ^{1,2,*}, Yuya Takekuma ^{1,2}, Tsuyoshi Ochiai ^{2,3,4}  and Morio Nagata ^{1,*}

¹ Graduate School of Engineering, Tokyo University of Science, 12-1, Ichigayafunagawara, Shinjuku-ku, Tokyo 162-0826, Japan; tytakekuma@gmail.com

² Photocatalyst Group, Research and Development Department, Local Independent Administrative Agency Kanagawa Institute of Industrial Science and Technology (KISTEC), 407 East Wing, Innovation Center Building, KSP, 3-2-1 Sakado, Takatsu-ku, Kawasaki, Kanagawa 213-0012, Japan; pg-ochiai@newkast.or.jp

³ Materials Analysis Group, Kawasaki Technical Support Department, KISTEC, Ground Floor East Wing, Innovation Center Building, KSP, 3-2-1 Sakado, Takatsu-ku, Kawasaki, Kanagawa 213-0012, Japan

⁴ Photocatalysis International Research Center, Tokyo University of Science, 2641 Yamazaki, Noda, Chiba 278-8510, Japan

* Correspondence: rikadai2018@gmail.com (R.E.); nagata@ci.kagu.tus.ac.jp (M.N.); Tel.: +81-3-5228-8311 (R.E. & M.N.); Fax: +81-3-5261-4631 (R.E. & M.N.)

Received: 25 July 2018; Accepted: 28 August 2018; Published: 30 August 2018



Abstract: Interfacial charge-transfer (ICT) transitions involved in charge-separation mechanisms are expected to enable efficient photovoltaic conversions through one-step charge-separation processes. With this in mind, the charge-transfer complex fabricated from TiO₂ nanoparticles and 7,7,8,8-tetracyanoquinodimethane (TCNQ) has been applied to dye-sensitized solar cells. However, rapid carrier recombination from the conduction band of TiO₂ to the highest occupied molecular orbital (HOMO) of TCNQ remains a major issue for this complex. In this study, to inhibit surface-complex recombinations, we prepared Nb-doped TiO₂ nanoparticles with different atomic ratios for enhanced electron transport. To investigate the effects of doping on electron injection through ICT transitions, these materials were examined as photoelectrodes. When TiO₂ was doped with 1.5 mol % Nb, the Fermi level of the TiO₂ electrode shifted toward the conduction band minimum, which improved electron back-contact toward the HOMO of TCNQ. The enhancement in electron transport led to increases in both short circuit current and open circuit voltage, resulting in a slight (1.1% to 1.3%) improvement in photovoltaic conversion efficiency compared to undoped TiO₂. Such control of electron transport within the photoelectrode is attributed to improvements in electron injection through ICT transitions.

Keywords: photovoltaic conversion; interfacial charge-transfer transition; 7,7,8,8-tetracyanoquinodimethane; Nb-doped TiO₂

1. Introduction

Interfacial charge-transfer (ICT) transitions between inorganic semiconductors and π -conjugated organic compounds are characteristic electronic transitions that enable direct photoinduced charge separation. Due to this feature, ICT transitions are applicable to photovoltaic conversions [1]. To date, dicyanomethylene-based compounds, such as tetracyanoethylene (TCNE) and 7,7,8,8-tetracyanoquinodimethane (TCNQ), form surface complexes with TiO₂ that have been reported to absorb visible light due to ICT transitions from the π -conjugated system to the conduction band of TiO₂ [2–4]. Although photovoltaic effects due to direct electron injection have been investigated

using these surface complexes as photoanodes in photoelectrochemical cells, the photovoltaic conversion efficiencies under AM1.5 illumination are quite low (under 2%) when compared to those of dye-sensitized solar cells (DSSCs) [5].

To date, photovoltaic conversions and electron injections between surface complexes, such as bis(dicyanomethylene) compounds (TCNX) [TCNE, TCNQ, and 11,11,12,12-tetracyanonaphtho-2,6-quinodimethane (TCNAQ)] and TiO₂, have been studied theoretically by Fujisawa et al. using density functional theory (DFT) on the basis of Marcus theory, which revealed that the structure and formation mechanism of the surface complex need to be considered to control interfacial electronic transitions and carrier recombinations by adjusting the electron affinity of TCNX [6–8]. In addition, they also demonstrated that carrier recombinations from the conduction band of TiO₂ to the highest occupied molecular orbital (HOMO) levels of these compounds occur quite rapidly, which, as geminate recombinations, are more severe than in DSSCs. Hence, the rapid carrier recombinations of surface complexes hinder the use of ICT transitions in photovoltaic conversion [9] and is the most significant problem faced.

To overcome rapid electron recombination, the properties of surface complexes require further investigation through different approaches that include investigating the interactions between TCNX and modified-TiO₂ photoanodes. Zaban et al. studied the suppression of electron recombination in surface complexes aided by a thin SrTiO₃ coating layer on TiO₂ that improved electron injection and electron transport [10]. On the other hand, many researchers reported that the TiO₂ photoanode in a DSSC is one of the most important components affecting photovoltaic performance because it acts as the support for dye molecules as well as the electron-transport region. Furthermore, TiO₂ can, in principal, be n-type-doped to enhance charge collection and electron-transport efficiency within the TiO₂ layer [11].

Among n-type-doped TiO₂ systems, Nb-doped TiO₂ photoanodes have been studied to improve electron conductance and injection because Nb has one more electron than Ti (IV) [12–18]. Recently, Lin et al. reported the influence of TiO₂ doped with Group V-b metal atoms on the photovoltaic performance of dye-sensitized solar cells [18]. Although V, Nb, and Ta belong to the same group (V-b) and have one more electron than Ti, DSSCs based on Nb-doped TiO₂ showed the best photovoltaic performance as a result of the creation of donor levels, which increased the concentration of the carriers. According to this study, the charge transport and conductivity for Nb-doped TiO₂ were superior to those of V- and Ta-doped TiO₂. Therefore, Nb is a superior doping element.

In this study, to inhibit rapid electron recombinations in surface complexes, we examined the effects of Nb-doped TiO₂ electrodes with TCNQ on photovoltaic performance. The effects of different amounts of Nb-doping on the photovoltaic properties of surface complexes were evaluated by means of incident photon-to-current efficiency (IPCE) spectroscopy and by acquiring current-density–voltage (J-V) curves. TiO₂ doped with 1.5 mol % Nb exhibited improved J_{sc} and V_{oc} values, resulting in a 17% improvement in photoconversion efficiency compared to undoped TiO₂.

2. Results and Discussion

2.1. Structural Characterization of Nb-Doped TiO₂

Nb-doped TiO₂ nanoparticles were formed by a hydrothermal method. Figure 1 displays the X-ray diffraction (XRD) patterns of undoped and Nb-doped TiO₂ samples with varying Nb contents. The anatase and rutile phases of TiO₂ are distinct, and the intensity of the peak corresponding to the anatase phase increased with increasing Nb content in the sample, while that of the rutile phase decreased (Figure 1a). Hence, doping the TiO₂ lattice with Nb was observed to enhance the growth of the anatase TiO₂ phase while hindering the formation of the rutile TiO₂ phase [19]. The average crystallite size of each phase was calculated by the Scherrer-equation [20]:

$$D = \frac{k\lambda}{B \cos \theta} \quad (1)$$

where D is the crystallite size, k is a dimensionless shape factor that has a typical value of 0.94, λ is the Cu-K α X-ray wavelength (1.5406 Å), θ is the Bragg angle in degrees, and B is the full-width-at-half-maximum (FWHM) of the peak. The anatase and rutile crystallinities were determined from their (101) and (110) peak heights, respectively; crystallite size are listed in Table S1. Incorporation of the Nb dopant into the TiO₂ structure typically decreased crystallite growth; indeed, the crystallite size of the anatase phase slowly decreased from 10.1 nm to 8.8 nm with increased doping, led by the effect of Nb on nucleation following doping into the TiO₂ lattice. A similar effect of different oxide additives on the TiO₂ phase transformation was reported by Yanagida et al. [19]. In addition, the diffraction peaks shifted to lower θ values with increasing Nb content as a result of the larger radius of Nb⁵⁺ (0.64 Å) compared to that of Ti⁴⁺ (0.61 Å) [15], in accordance with the Bragg equation: $\lambda = 2d\sin\theta$ (Figure 1b).

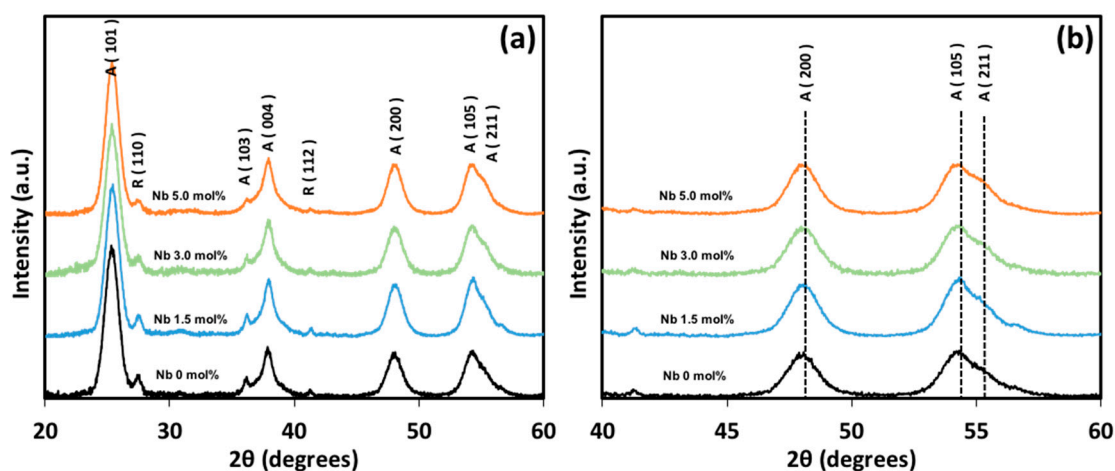


Figure 1. (a) X-ray diffraction (XRD) patterns of TiO₂ with varying Nb contents (A: Anatase, R: Rutile). (b) XRD patterns between 2θ values of 40° and 60°.

Figure 2 displays the X-ray photoelectron spectroscopy (XPS) spectra of the undoped and Nb-doped TiO₂ samples with varying Nb contents. Nb 3d_{3/2} and 3d_{5/2} peaks are evident in the spectra of the Nb-doped TiO₂ samples, and their intensities increased with increasing Nb content (Figure 2a). The Nb 3d_{3/2} and 3d_{5/2} peaks are located at binding energies of 209 and 206 eV, respectively. Nb-doping also caused the Ti 2p_{1/2} and 2p_{3/2} peaks to shift slightly toward higher binding energies, which is attributable to the higher electronegativity of Nb (1.6) compared to that of Ti (1.54) (Figure 2b) [15]. The peaks in the O 1s spectra correspond to Ti⁴⁺–O bonds; the positions of these peaks show similar trends to those observed for Ti due to increases in both lattice oxygen and Nb⁵⁺–O bonds in these samples. Figure 2d displays a double-band structure, with the main peak (29.4 eV) related to O 1s electron binding in TiO₂ and the other peak, at a higher binding energy (531 eV), attributed to OH groups on the surfaces of these samples. Typically, OH groups are beneficial for TCNQ anchoring [21].

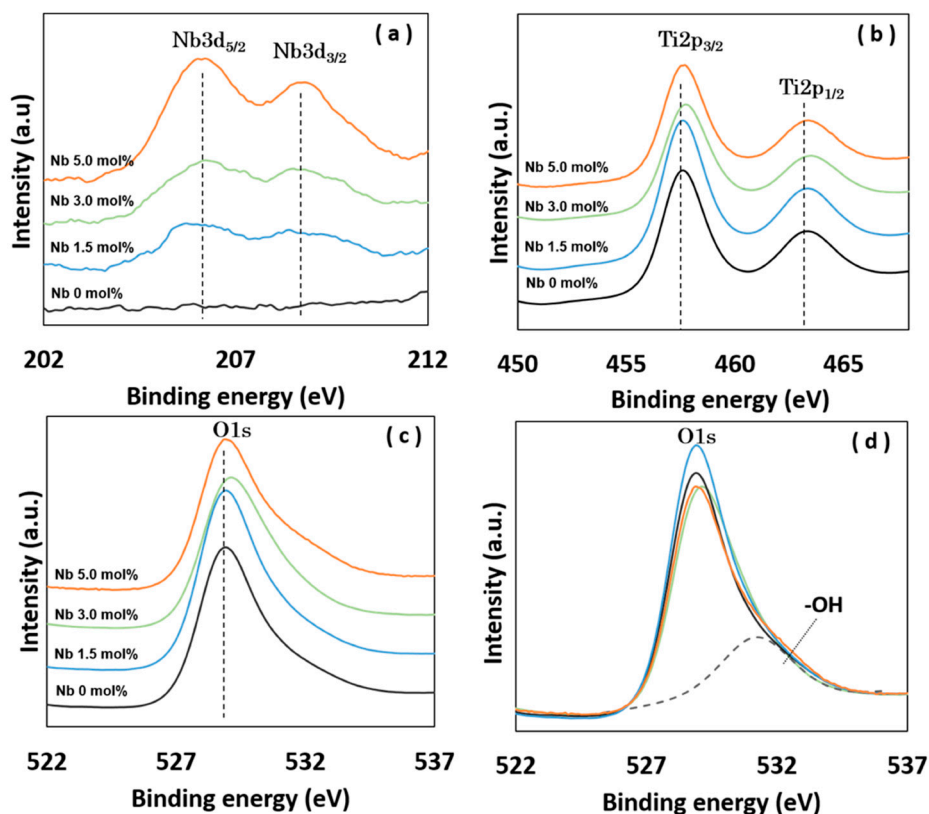


Figure 2. High-resolution (a) Nb 3d, (b) Ti 2p, and (c) O 1s X-ray photoelectron spectroscopy (XPS) spectra of TiO₂ with varying Nb contents. (d) O 1s spectral fitting, revealing the presence of peaks related to OH groups.

2.2. Optical Properties of Nb-Doped TiO₂

Examination of the electronic structures of the Nb-doped TiO₂ electrodes is essential to understand the ICT transition from the highest occupied molecular orbital (HOMO) of TCNQ to the conduction band of TiO₂. XPS and calculated E_g values for the valence band can provide electronic-potential information. The reflectance spectra displayed in Figure S1a enable the bandgaps of the samples to be determined. E_g values were calculated after converting the reflectance data into the equivalent absorption coefficients using Equation (1), as shown in Figure S1b and listed in Table 1. E_g increased from 3.06 eV to 3.14 eV as the Nb content was increased from 0 mol % to 5.0 mol %, which is ascribable to strong hybridization between the Ti 3d and Nb 3d states that forms a d-type conduction band [22]. The observed increase in bandgap with increasing Nb content can be also explained by the decrease in the amount of rutile phase TiO₂ formed (Table S1); indeed, the bandgap of anatase is 3.2 eV, which is larger than that of rutile (3.0 eV).

Table 1. Optical bandgap values for TiO₂ samples with different Nb contents.

Nb Content (mol %)	0	1.5	3.0	5.0
E_g (eV)	3.06	3.07	3.11	3.14
$E_{CBM}-E_F$ (eV)	0.46	0.37	0.41	0.64

Figure 3 shows the photoemission spectra of TiO₂ samples with different Nb contents, in which the binding energies are referenced against the Fermi energy level (E_F). Two peaks are evident in each photoemission spectrum, one centered at 6.4 eV and the other at 8.2 eV. These peaks are attributed to emissions from π - and σ -type O 2p orbitals, respectively. The positions of the valence band maxima

(VBMs) were directly determined from the photoemission spectra by linear extrapolation of the onsets of the valence-band emissions [12]. In the case of the undoped TiO₂ sample, the VBM was found to be located 2.6 eV below the Fermi level. With the optical bandgap determined to be 3.06 eV, we deduce that E_F is 0.46 eV lower than the energy of the conduction band minimum (E_{CBM}). The calculated positions of the conduction band minimum (CBM) with respect to the Fermi level are summarized in Table 1. The energy of the CBM of the 1.5 mol % Nb-doped TiO₂ was found to be 0.37 eV higher than that of the Fermi level, while that of the undoped TiO₂ was 0.46 eV higher (Table 1). The CBM of the sample containing 1.5 mol % Nb was therefore 0.09 eV lower in energy than that of undoped TiO₂. The observed lowering of the CBM of the sample containing 1.5 mol % and 3.0 mol % Nb due to donor levels induced by these dopants [18] is attributable to higher electron transitions between the Nb-doped TiO₂ electrode and the anchoring TCNQ. On the other hand, the CBM for the sample containing 5.0 mol % Nb exhibited a large offset between its CBM energy and E_F , compared to the undoped TiO₂, due to intra-band transport [15].

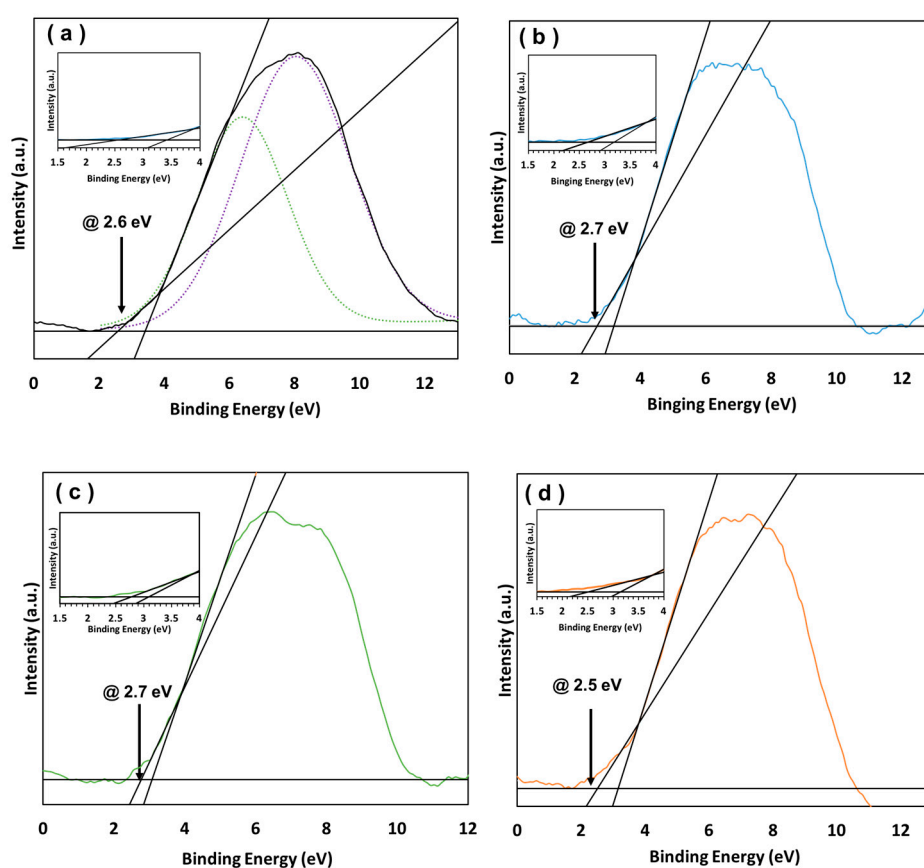


Figure 3. XPS spectra and valence-band maxima of the Nb-doped TiO₂ with Nb contents of (a) 0, (b) 1.5, (c) 3.0 mol %, and (d) 5.0 mol %. The Gaussian fitted electron emissions from the π (green) and σ (purple) O 2p orbitals are also shown in (a).

2.3. Photovoltaic Performance of Interfacial Charge-Transfer (ICT) Photoconversion Devices

The photovoltaic performance of ICT-transition devices based on the undoped and Nb-doped TiO₂ electrodes with varying Nb contents under solar illumination (AM 1.5 G, 100 mW/cm²) are displayed in Figure 4a, with the photovoltaic performance parameters summarized in Table 2. J_{sc} was observed to increase from 4.5 mA/cm² to 5.7 mA/cm² at an Nb content of 3.0 mol %, which is attributable to improved electronic transitions between the nanoparticles and the anchoring TCNQ associated with the negative CBM-energy shift (Table 1). On the other hand, V_{oc} increased slightly, from 0.40 V to 0.41 V, as the dopant content was increased to 1.5 mol % due to the increased gap between E_F and the

redox potential of the I^-/I^{3-} couple. This is also attributable to Nb-doped TiO_2 -surface passivation, according to electrochemical impedance spectroscopy (EIS) (Nyquist plots, Figure S2) [23,24]. However, increased Nb doping has a negative influence on photovoltaic behavior at levels over 5.0 mol %; indeed, V_{oc} decreased from 0.40 V to 0.36 V, which is ascribable to a detrimental conduction-band-edge effect. Indeed, the XRD result shows the decrease in rutile crystallization in 5.0 mol % Nb-doped TiO_2 (Table S1) led to defects in crystallization, and affected electron recombination such the degradation of V_{oc} parameter.

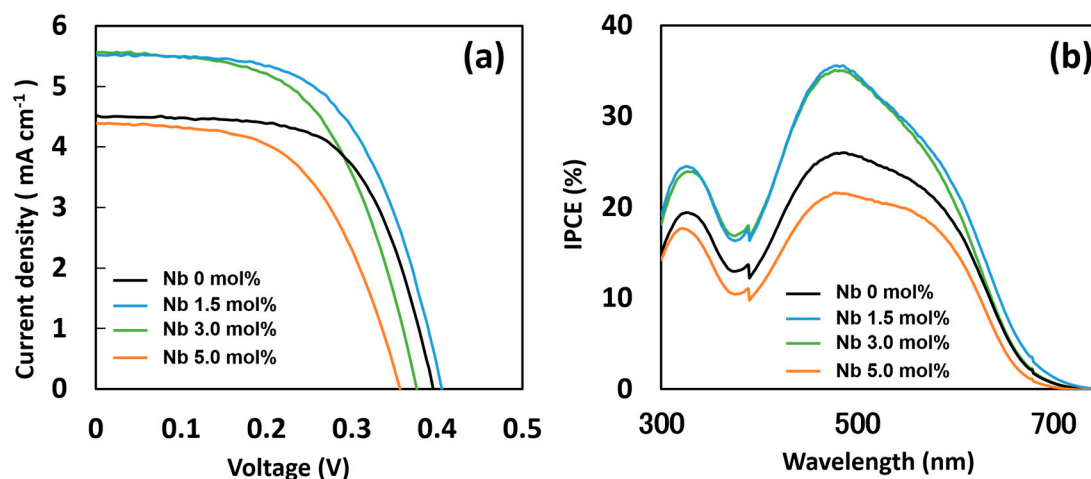


Figure 4. (a) Photocurrent-density–voltage curves and (b) incident photon-to-current conversion efficiency spectra of Interfacial charge-transfer (ICT) photoconversion devices based on the undoped and Nb-doped TiO_2 electrodes prepared in this study.

Table 2. Photovoltaic-performance parameters of Interfacial charge-transfer (ICT) photoconversion devices based on the undoped and Nb-doped TiO_2 electrodes prepared in this study.

Sample	J_{sc} (mA/cm ²)	V_{oc} (V)	FF (%)	H (%)
Nb 0 mol %	4.5	0.40	63	1.1
Nb 1.5 mol %	5.5	0.41	59	1.3
Nb 3.0 mol %	5.7	0.38	57	1.2
Nb 5.0 mol %	4.4	0.36	56	0.87

Figure 4b reveals that the device containing the 1.5 mol % Nb-doped TiO_2 electrode exhibits enhanced IPCE compared to that of the undoped electrode. Indeed, the absorption edge was observed to shift from 730 nm to 750 nm. Nb has been reported to create oxygen vacancies in TiO_2 that act as active sites, resulting in a photoresponse red shift [25]. However, the lowest IPCE was obtained in the device containing the 5.0 mol % Nb-doped TiO_2 electrode, as revealed by the J-V curves.

According to previous studies on the fabrication of DSSCs based on TiO_2 doped with Nb at concentrations up to 5.0 mol %, Feng et al. and Huang et al. reported that the highest photovoltaic efficiency was observed for Nb concentrations of 2.0 mol % and 5.0 mol %, respectively [15,16]. However, our results demonstrated that Nb-doping of 1.5 mol % produced the highest efficiency. Considering the behavior of J_{sc} with doping, we can conclude that the optimum Nb concentration for reaching the best efficiency is in the range of 1.5–3.0 mol %. In addition, the error bar of photovoltaic efficiency in this study is shown in Figure S3.

3. Experimental Section

3.1. Preparation of Nb-Doped TiO₂

The Nb-doped TiO₂ nanoparticles were synthesized following the procedure described by Nikolay et al. [12]. These syntheses used Ti and Nb precursors and hydrothermal processes. To prepare Nb-doped TiO₂ (0, 1.5, 3.0, or 5.0 mol %) nanoparticles, 16.4 mL of titanium tetraisopropoxide (Kanto Chemical Co., Tokyo, Japan) was mixed with 0, 60, 120, or 200 µL of niobium ethoxide (Wako Co., Tokyo, Japan), respectively, after which 2.64 mL of acetic acid (Kanto Chemical Co., Tokyo, Japan) was added under stirring condition with a Teflon stirrer blade for 15 min at room temperature. The mixture was dropped into 68.4 mL of deionized water while stirred at about 800 rpm. After stirring for 1 h, 2.35 mL of 65% nitric acid (Kanto Chemical Co., Tokyo, Japan) was added to the solution. The solution temperature was increased to 80 °C over 40 min and then held at 80 °C for 80 min under reflux conditions with intensive stirring. The nanoparticles were hydrothermally grown using the prepared colloidal solution in a Teflon-lined mini-autoclave at 180 °C for 12 h, after which 0.52 mL of 65% nitric acid was added to the colloidal solution, followed by ultrasonication with stirring for 1 h. The prepared mixture was finally washed three times with ethanol by centrifugation.

3.2. Cell Fabrication

The Nb-doped TiO₂ pastes were synthesized following the procedure reported by Ito et al. [26]. The final screen-printing pastes correspond to 18 wt % TiO₂, 9 wt % ethyl cellulose and 73 wt % terpineol. Two kinds of pure ethyl cellulose (EC) powders, i.e., EC (10 mPas, Kanto Chemical Co., Tokyo, Japan) and EC (45 mPas, Kanto Chemical Co., Tokyo, Japan) were dissolved before usage in ethanol to yield 10 wt % solutions. Then, 0.325 g of EC (10 mPas) and 0.175 g of EC (45 mPas) of these 10 wt % ethanolic mixtures were added to a round-bottomed rotovap flask containing 1 g pure TiO₂ (obtained from a previously prepared precipitate) and 4.05 g of terpineol (Kanto Chemical Co., Tokyo, Japan), and diluted with approximately 100 ml of ethanol. This mixture was then ultrasonicated for 48 h. Ethanol and water were removed from these TiO₂/ethyl cellulose solutions using a rotary-evaporator. The final formulations of the pastes were made with a three-roll mill (Exakt, Nagase Screen Printing Research Co., Aichi, Japan). The Nb-doped TiO₂ electrodes were fabricated by screen-printing pastes onto glass substrates coated with transparent conducting F-doped SnO₂ (FTO), Nippon Sheet Glass Co., Tokyo, Japan) with a sheet resistance of 10 Ω sq⁻¹, followed by sintering at 500 °C for 30 min. The thickness of the TiO₂ electrode was set to 8 µm.

The TiO₂ electrodes were immersed in a 1 mM solution of TCNQ (Tokyo Kasei Kogyo Co., Tokyo, Japan) in acetonitrile at 60 °C for 24 h. Photovoltaic cells were fabricated using the TCNQ-treated TiO₂ electrode (active area: 4 mm × 4 mm), a Pt-sputtered FTO glass counter electrode (Geomatec Co., Kanagawa, Japan), an I⁻/I₃⁻ redox couple electrolyte (1 M LiI (Sigma-Aldrich Co., St. Louis, MO, USA) and 0.025 M I₂ (Kanto Chemical Co.) in acetonitrile), and a spacer film (thickness: 30 µm).

3.3. Characterization

Incident photon-to-current efficiency (IPCE) spectra were acquired using a Hypermonolight system (M10, Bunkoukeiki Co., Tokyo, Japan) with a calibrated silicon photodiode (Bunkoukeiki Co., Tokyo, Japan). Current-density–voltage (J-V) curves were recorded using a potentiostat (1287A potentiostat/galvanostat, Ametek Co., St. Berwyn, PA, USA) under 100 mW/cm² AM 1.5 G simulated sunlight produced by a solar simulator (Yamashita Denso Co., Tokyo, Japan). Electrochemical impedance spectroscopy (EIS) was performed using a potentiostat equipped with calculation software (1255B frequency-response analyzer, Ametek Co, Tokyo, Japan). The thicknesses of the films were measured using a surface roughness profilometer (SURFCOM1440D, Accretech Co., Tokyo, Japan). Crystal structures were determined by X-ray diffraction (XRD, Ultima X-ray diffractometer, Rigaku Co., Yamanashi, Japan). The electronic structures and chemical states of the TiO₂ electrodes were investigated by X-ray photoelectron spectroscopy (XPS) (JPS-9010MC,

Nihondensi Co., Tochigi, Japan). The binding energies were calibrated against the C 1s peak at 284.60 eV. For all XPS measurements, undoped TiO₂ and Nb-doped TiO₂ were deposited on carbon sheets. UV-vis spectroscopy was performed using a U-3900H spectrometer (Hitachi Co., Tokyo, Japan) in reflectance mode, and the spectra were analyzed using the Kubelka-Munk formalism to convert reflectance into the equivalent absorption coefficient, α_{KM} [27–29]:

$$\alpha_{KM} = \frac{(1 - R_{\infty})^2}{2R_{\infty}} \quad (2)$$

where: R_{∞} is the reflectance of an infinitely thick sample with respect to the reference at each wavelength.

4. Conclusions

In this study, we examined the abilities of Nb-doped TiO₂ electrodes with 7,7,8,8-tetracyanoquinodimethane (TCNQ) to inhibit electron recombinations in surface-complexes. The 1.5 mol % Nb-doped TiO₂ electrode exhibited improved photovoltaic performance and superior short circuit current and open circuit voltage, resulting in 1.3% photoconversion efficiency, which is 17% higher than that of the undoped photoelectrode. This improvement is ascribed to enhanced electron injection resulting from a shift in the Fermi level of the TiO₂ electrode toward the conduction band minimum, and the effect of passivation, as revealed by Electrochemical impedance spectroscopy. As expected, these experimental data for Nb-doped TiO₂ with TCNQ reveal that semiconductor modification can be used to achieve efficient photovoltaic conversion through Interfacial charge-transfer transitions by suppressing surface-complex carrier recombinations and improving electron transport.

Supplementary Materials: The following are available online at <http://www.mdpi.com/2073-4344/8/9/367/s1>. Table S1: Crystallite sizes of TiO₂ samples with various Nb contents; Table S2: Fitted EIS spectra of TiO₂ samples with varying Nb contents. Figure S1: (a) Reflectance spectra and (b–e) optical bandgaps of TiO₂ samples with varying Nb contents; Figure S2: Electrochemical impedance spectra (Nyquist plots) of the undoped and Nb-doped TiO₂ electrodes; Figure S3: Error bars for Conversion efficiency of DSSCs employing different Nb dopants.

Author Contributions: R.E., Y.T., T.O., and M.N. participated in the study design and conducted the experiments. Data were collected and analyzed by R.E. and Y.T. The manuscript was written by R.E., M.N. and T.O. provided valuable input and advice regarding the manuscript.

Funding: This research received no external funding.

Conflicts of Interest: The authors declare no conflicts of interest.

References

1. Fujisawa, J.-I. Large Impact of Reorganization Energy on Photovoltaic Conversion Due to Interfacial Charge-Transfer Transitions. *Phys. Chem. Chem. Phys.* **2015**, *17*, 12228–12237. [[CrossRef](#)] [[PubMed](#)]
2. Xagas, A.P.; Bernard, M.C.; Hugot-Le Goff, A.; Spyrellis, N.; Loizos, Z.; Falaras, P. Surface Modification and Photosensitisation of TiO₂ Nanocrystalline Films with Ascorbic Acid. *J. Photochem. Photobiol. A* **2000**, *132*, 115–120. [[CrossRef](#)]
3. Tae, E.L.; Lee, S.H.; Lee, J.K.; Yoo, S.S.; Kang, E.J.; Yoon, K.B. A Strategy to Increase the Efficiency of the Dye-Sensitized TiO₂ Solar Cells Operated by Photoexcitation of Dye-to-TiO₂ Charge-Transfer Bands. *J. Phys. Chem. B* **2005**, *109*, 22513–22522. [[CrossRef](#)] [[PubMed](#)]
4. Manzhos, S.; Jono, R.; Yamashita, K.; Fujisawa, J.-I.; Nagata, M.; Segawa, H. Study of Interfacial Charge Transfer Bands and Electron Recombination in the Surface Complexes of TCNE, TCNQ, and TCNAQ with TiO₂. *J. Phys. Chem. C* **2011**, *115*, 21487–21493. [[CrossRef](#)]
5. Manzhos, S.; Fujisawa, J.-I.; Segawa, H.; Yamashita, K. Isotopic Substitution as a Strategy to Control Non-Adiabatic Dynamics in Photoelectrochemical Cells: Surface Complexes between TiO₂ and Dicyanomethylene Compounds. *J. Appl. Phys.* **2012**, *51*, 10NE03. [[CrossRef](#)]

6. Fujisawa, J.-I.; Nagata, M.; Hanaya, M. Charge-Transfer Complex Versus [Sigma]-Complex Formed between TiO₂ and Bis (Dicyanomethylene) Electron Acceptors. *Phys. Chem. Chem. Phys.* **2015**, *17*, 27343–27356. [[CrossRef](#)] [[PubMed](#)]
7. Michinobu, T.; Satoh, N.; Cai, J.; Li, Y.; Han, L. Novel Design of Organic Donor-Acceptor Dyes without Carboxylic Acid Anchoring Groups for Dye-Sensitized Solar Cells. *J. Mater. Chem. C* **2014**, *2*, 3367–3372. [[CrossRef](#)]
8. Fujisawa, J.-I.; Hanaya, M. Electronic Structures of TiO₂-TCNE, -TCNQ, and -2,6-TCNAQ Surface Complexes Studied by Ionization Potential Measurements and DFT Calculations: Mechanism of the Shift of Interfacial Charge-Transfer Bands. *Chem. Phys. Lett.* **2016**, *653*, 11–16. [[CrossRef](#)]
9. Wang, Y.; Hang, K.; Anderson, N.A.; Lian, T. Comparison of Electron Transfer Dynamics in Molecule-to-Nanoparticle and Intramolecular Charge Transfer Complexes. *J. Phys. Chem. B* **2003**, *107*, 9434–9440. [[CrossRef](#)]
10. Hod, I.; Shalom, M.; Tachan, Z.; Rühle, S.; Zaban, A. SrTiO₃ Recombination-Inhibiting Barrier Layer for Type II Dye-Sensitized Solar Cells. *J. Phys. Chem. C* **2010**, *114*, 10015–10018. [[CrossRef](#)]
11. Zhang, S.; Yang, X.; Numata, Y.; Han, L. Highly Efficient Dye-Sensitized Solar Cells: Progress and Future Challenges. *Energy Environ. Sci.* **2013**, *6*, 1443–1464. [[CrossRef](#)]
12. Nikolay, T.; Larina, L.; Shevaleevskiy, O.; Ahn, B.A. Electronic Structure Study of Lightly Nb-Doped TiO₂ Electrode for Dye-Sensitized Solar Cells. *Energy Environ. Sci.* **2011**, *4*, 1480–1486. [[CrossRef](#)]
13. Ghartavol, H.M.; Mohammadi, M.R.; Afshar, A.; Chau-Nan Hong, F.; Jeng, Y.-R. Efficient Dye-Sensitized Solar Cells Based on CNT-Derived TiO₂ Nanotubes and Nb-Doped TiO₂ Nanoparticles. *RSC Adv.* **2016**, *6*, 101737–101744. [[CrossRef](#)]
14. Liu, W.; Wang, H.-G.; Wang, X.; Zhang, M.; Guo, M. Titanium Mesh Supported TiO₂ Nanowire Arrays/Nb-Doped TiO₂ Nanoparticles for Fully Flexible Dye-Sensitized Solar Cells with Improved Photovoltaic Properties. *J. Mater. Chem. C* **2016**, *4*, 11118–11128. [[CrossRef](#)]
15. Su, H.; Huang, Y.-T.; Chang, Y.-H.; Zhai, P.; Hau, N.Y.; Cheung, P.C.H.; Yeh, W.-T.; Wei, N.T.-C.; Feng, S.-P. The Synthesis of Nb-Doped TiO₂ Nanoparticles for Improved-Performance Dye Sensitized Solar Cells. *Electrochim. Acta* **2015**, *182*, 230–237. [[CrossRef](#)]
16. Lü, X.; Mou, M.X.; Wu, J.; Zhang, D.; Zhang, L.; Huang, F.; Xu, F.; Huang, S. Improved-Performance Dye-Sensitized Solar Cells Using Nb-Doped TiO₂ Electrodes: Efficient Electron Injection and Transfer. *Adv. Funct. Mater.* **2010**, *20*, 509–515. [[CrossRef](#)]
17. Kim, S.G.; Ju, M.J.; Choi, I.T.; Choi, W.S.; Choi, H.-J.; Baek, J.-B.; Kim, H.K. Nb-Doped TiO₂ Nanoparticles for Organic Dye-Sensitized Solar Cells. *RSC Adv.* **2013**, *3*, 16380–16386. [[CrossRef](#)]
18. Liu, J.; Duan, Y.; Zhou, X.; Lin, Y. Influence of V_B Group Doped TiO₂ on Photovoltaic Performance of Dye-Sensitized Solar Cells. *Appl. Surf. Sci.* **2013**, *277*, 231–236. [[CrossRef](#)]
19. Hishita, S.; Mutoh, I.; Koumoto, K.; Yanagida, H. Inhibition Mechanism of the Anatase-Rutile Phase Transformation by Rare Earth Oxides. *Ceram. Int.* **1983**, *9*, 61–67. [[CrossRef](#)]
20. Cullity, B.D. Elements of X-Ray Diffraction. *Am. J. Phys.* **1957**, *25*, 394–395. [[CrossRef](#)]
21. Jono, R.; Fujisawa, J.-I.; Segawa, H.; Yamashita, K. Theoretical Study of the Surface Complex between TiO₂ and TCNQ Showing Interfacial Charge-Transfer Transitions. *J. Phys. Chem. Lett.* **2011**, *2*, 1167–1170. [[CrossRef](#)] [[PubMed](#)]
22. Taro, H.; Hideyuki, K.; Koichi, Y.; Hiroyuki, N.; Yutaka, F.; Shoichiro, N.; Naoomi, Y.; Akira, C.; Hiroshi, K.; Masaharu, O.; et al. Electronic Band Structure of Transparent Conductor: Nb-Doped Anatase TiO₂. *Appl. Phys. Express* **2008**, *1*, 111203.
23. Bisquert, J. Theory of the Impedance of Electron Diffusion and Recombination in a Thin Layer. *J. Phys. Chem. B* **2002**, *106*, 325–333. [[CrossRef](#)]
24. Zhang, Z.; Zakeeruddin, S.M.; O'Regan, B.C.; Humphry-Baker, R.; Grätzel, M. Influence of 4-Guanidinobutyric Acid as Coadsorbent in Reducing Recombination in Dye-Sensitized Solar Cells. *J. Phys. Chem. B* **2005**, *109*, 21818–21824. [[CrossRef](#)] [[PubMed](#)]
25. Karvinen, S. The Effects of Trace Elements on the Crystal Properties of TiO₂. *Solid State Sci.* **2003**, *5*, 811–819. [[CrossRef](#)]
26. Ito, S.; Murakami, T.N.; Comte, P.; Liska, P.; Grätzel, C.; Nazeeruddin, M.K.; Grätzel, M. Fabrication of Thin Film Dye Sensitized Solar Cells with Solar to Electric Power Conversion Efficiency over 10%. *Thin Solid Films* **2008**, *516*, 4613–4619. [[CrossRef](#)]

27. Kubelka, P. New Contributions to the Optics of Intensely Light-Scattering Materials. Part I. *J. Opt. Soc. Am.* **1948**, *38*, 448–457. [[CrossRef](#)]
28. Yang, L.; Kruse, B. Revised Kubelka–Munk Theory. I. Theory and Application. *J. Opt. Soc. Am. A* **2004**, *21*, 1933–1941. [[CrossRef](#)]
29. Yang, L.; Miklavcic, S.J. Revised Kubelka–Munk Theory. III. A General Theory of Light Propagation in Scattering and Absorptive Media. *J. Opt. Soc. Am. A* **2005**, *22*, 1866–1873. [[CrossRef](#)]



© 2018 by the authors. Licensee MDPI, Basel, Switzerland. This article is an open access article distributed under the terms and conditions of the Creative Commons Attribution (CC BY) license (<http://creativecommons.org/licenses/by/4.0/>).